Geochimica et Cosmochimica Acta 348 (2023) 27–40

Contents lists available at ScienceDirect

Geochimica et Cosmochimica Acta

journal homepage: www.elsevier.com/locate/gca

Micropore sites in ferrihydrite are responsible for its higher affinity towards As(III) relative to As(V)

Qian Zheng [a], Shuxin Tu [a], Yiwen Chen [b], Hongjun Zhang [b], William Hartley [c], Bangjiao Ye [b], Lu Ren [d], Juan Xiong [a], Wenfeng Tan [a], Andreas Kappler [e], Jingtao Hou [a,*]

[a] State Environmental Protection Key Laboratory of Soil Health and Green Remediation, Hubei Key Laboratory of Soil Environment and Pollution Remediation, College of Resources and Environment, Huazhong Agricultural University, Wuhan 430070, China
[b] State Key Laboratory of Particle Detection and Electronics, University of Science and Technology of China, Hefei 230026, China
[c] Agriculture and Environment Department, Harper Adams University, Newport, Shropshire TF10 8NB, United Kingdom
[d] School of Civil Engineering, Suzhou University of Science and Technology, Suzhou 215009, China
[e] Geomicrobiology, Department of Geosciences, University of Tuebingen, Tuebingen 72076, Germany

ARTICLE INFO

Article history:
Received 19 July 2022
Accepted 2 March 2023
Available online 7 March 2023
Associate editor: Mario Villalobos

Keywords:
Iron (oxyhydr)oxide
Immobilization
Arsenite
Arsenate
Micropore site

ABSTRACT

Poorly-crystalline ferrihydrite is ubiquitous in the environment and contributes to controlling the fate of arsenic in sediments and soils. Although there is evidence that ferrihydrite has a higher affinity towards As(III) relative to As(V), little is known about how and why As(III) is readily immobilized by ferrihydrite. In this study, ferrihydrite was employed to evaluate the As(III) and As(V) adsorption behavior. The properties of ferrihydrite such as morphology, pore size distribution, arsenic adsorption species, and adsorption energies of arsenic at different sites were carefully examined using TEM-EDS mapping, positron annihilation lifetime (PAL) spectroscopy, X-ray absorption spectroscopy (XAS), N_2 adsorption isotherms, and theoretical calculations of density function theory (DFT). Batch adsorption experiments revealed that the maximum adsorption of As(III) (839.7 μmol g^{-1}) on ferrihydrite, fitted by Langmuir model, was considerably larger than that of As(V) (372.4 μmol g^{-1}). PAL characterization and pore size distribution analysis demonstrated that ferrihydrite had an abundance of vacancy cluster-like micropores, which consisted of 10–20 atom deficiencies ($V_{10\text{-}20}$). The calculated hydrated ion size of As(III) species (4.22 Å) at pH 6.0 was smaller than the size of As(V) (5.90 Å). The higher As(III) adsorption to ferrihydrite was attributed to its surface adsorption sites as well as its abundant micropore adsorption sites, which are available only to As(III) due to their size matching well with the size of the ferrihydrite micropores, thus significantly contributing to greater As(III) immobilization.

1. Introduction

Iron (Fe)-bearing (oxyhydr)oxides are common constituents of sediments and soils. Because of their large surface areas, as well as their high reactivities, iron (oxyhydr)oxides extensively participate in biogeochemical processes, including adsorption, oxidation, and reduction of nutrients and toxic metals (Boland et al., 2011; Bose and Sharma, 2002; Bylaska et al., 2019; Gim et al., 2007; Weber et al., 2006). There are numerous types of iron (oxyhydr)oxides (e.g., ferrihydrite, goethite, and hematite) in natural environments (Cornell and Schwertmann, 2003), and their microstructures are rather different, which enables them to exhibit unique reactivity (Parkinson, 2016), thereby significantly affecting the migration and fate of pollutants, especially for the carcinogenic element arsenic, a metalloid commonly found in polluted groundwater and soils (Deschamps et al., 2005; Dixit and Hering, 2003; Fritzsche et al., 2011; Liu et al., 2015; Neumann et al., 2013; Tan et al., 2022; Zhu et al., 2017).

Ferrihydrite is a poorly nano-crystalline iron oxyhydroxide that has an important contribution in controlling the fate of arsenic due to its large adsorption affinity and high abundance (Grafe et al., 2002; Huang et al., 2011; Jambor and Dutrizac, 1998; Jia et al., 2006; Zhao et al., 2011). In general, the oxyanions of arsenite [As(III), e.g., H_3AsO_3] and arsenate [As(V), e.g., $HAsO_4^{2-}$ and $H_2AsO_4^-$] are the two common inorganic arsenic species in arsenic polluted groundwater and pore water in the unsaturated zone, although their potential bioavailability and mobility have significant differences. Compared to As(V), As(III) is regarded as being more toxic and having a weaker affinity to iron (oxyhydr)oxides (Gim et al.,

* Corresponding author.
E-mail address: houjt87@163.com (J. Hou).

https://doi.org/10.1016/j.gca.2023.03.007
0016-7037/

2007; Guo et al., 2007; Meng et al., 2002; Tang et al., 2011). Some researchers have therefore suggested oxidation of As(III) coupled to the adsorption of the formed As(V) to binary metal oxides (e.g., Fe-Mn) as a possible strategy for efficient removal of As(III) from groundwater (Chang et al., 2010; Li et al., 2012; Zhang et al., 2012, 2007a, 2007b; Zheng et al., 2021, 2020). Nevertheless, other studies have observed a preferred adsorption of As(III), rather than As(V), on poorly crystalline ferrihydrite surfaces (Adra et al., 2016; Grafe et al., 2002; Raven et al., 1998; Zheng et al., 2020; Zhu et al., 2011). For example, Zhang et al. (2014, 2012) examined the adsorption performance of ferrihydrite for As(III) and As(V) removal. They found that the maximum adsorption of As(III) on ferrihydrite was ~2 times larger than that of As(V). Qi and Pichler (2014) also observed that ferrihydrite showed high As(III) adsorption capacity relative to that of As(V) in a wide pH range of 4–10. Several efforts have been made to explore the underlying mechanism of As(III) and As(V) immobilization on ferrihydrite. For example, structural incorporation of arsenate and formation of As^{3+} clusters were shown to contribute to As(III) and As(V) immobilization (Bolanz et al., 2013; Majzlan et al., 2014; Schindler et al., 2022). The binding energies of different As-Fe inner-sphere surface complexes were reported to be different for As(III) and As(V) species (Dzade and De Leeuw, 2018), i.e., the formation of bidentate binuclear (BB) corner-sharing As-Fe complexes was more energetically favorable than that of monodentate mononuclear As-Fe complexes for both As(III) and As(V) species. This observation was in agreement with the results of extended X-ray absorption fine structure (EXAFS) analysis (Manning et al., 1998; Ona-nguema et al., 2005; Waychunas et al., 1993). Moreover, surface protonation-deprotonation processes affected the adsorption energies of outer- and inner-sphere complexes of As(III) and As(V) species on the (110) surface of ferrihydrite (Dzade and De Leeuw, 2018).

Although the structure of ferrihydrite and the adsorption behavior of arsenic on ferrihydrite have been extensively investigated in the past decades (Adra et al., 2016; Huang et al., 2011; Jia et al., 2006; Maillot et al., 2011; Michel et al., 2007; Ona-nguema et al., 2005; Qi and Pichler, 2016; Tobler et al., 2019; Waychunas et al., 1996; Weatherill et al., 2016; Zhao et al., 2011), it is still unclear why As(III), rather than As(V), shows a higher immobilization potential by ferrihydrite. Elucidating the underlying mechanism of the different affinities of ferrihydrite towards As(III) and As(V) is very important for understanding the migration and fate of arsenic in contaminated soils and groundwaters, which also aids in designing high efficient iron oxide adsorbents for treating arsenic-contaminated groundwater.

Herein, poorly crystalline ferrihydrite was employed to evaluate the adsorption capacity for As(III) and As(V) removal. The properties of ferrihydrite, including morphology, pore size distribution, and the identity of adsorbed arsenic species and adsorption complexes were carefully examined. Density function theory (DFT) calculation was used to investigate the bond energies of arsenic adsorbed on different active sites of ferrihydrite. For the first time, we combined both theoretical and experimental evidence to demonstrate that the abundant micropore textures in ferrihydrite play a vital role in increasing As(III) adsorption, which is attributed to the efficient access to the micropore sites by the oxyanion of As(III) (e.g., H_3AsO_3) due to its small size.

2. Experimental section

2.1. Materials

Arsenic trioxide (As_2O_3) and $Na_2HAsO_4{\cdot}7H_2O$ were used to prepare As(III) and As(V) stock solutions. 3-Morphonopropanesulfonic acid (MOPS) was used as buffer in the reaction system. All reagents were of analytical grade and used without further treatment.

2.2. Mineral preparation

Ferrihydrite was synthesized using a precipitation approach according to previous studies (Schwertmann and Cornell, 2000; Zhang et al., 2007b). First, a NaOH solution (1 M) was slowly added into 500 mL of $Fe(NO_3)_3{\cdot}9H_2O$ (0.1 M) and mixed using a magnetic stirrer until the solution pH was stable between 7 and 8. After 2 h, the precipitate was washed several times until the conductivity was lower than 20 mS cm^{-1}. Finally, the powder was freeze-dried and stored at 4 °C. Hematite was described to have almost no micropores (Wang et al., 2013). Manganese oxide was reported to have strong oxidation capacity toward As(III) (Manning et al., 2002; Villalobos et al., 2014). In this study, hematite was therefore used as reference sample to reveal the effect of micropore sites on arsenic adsorption, and manganese oxide was employed to observe the transformation of As(III) to As(V) for comparison. Hematite and Mn oxide samples were prepared according to methods described in the literature (Hou et al., 2014; Schwertmann and Cornell, 2000). Further details of mineral preparation procedures are presented in Text S1 (Supplementary Material).

2.3. Mineral characterization

The structure, morphology, micropore distribution, and surface elemental species of ferrihydrite before and after reaction with arsenic were analyzed by X-ray diffraction (XRD), scanning electronic microscopy (SEM), high resolution-transmission electronic microscopy (HR-TEM) and energy dispersion spectrum (EDS) mapping, N_2 adsorption/desorption curves, and X-ray photoelectron spectrometry (XPS). Speciation of arsenic adsorbed on ferrihydrite was determined using Fourier transform infrared spectroscopy (FTIR). The micropore size distribution was analyzed using nonlinear density functional theory (NLDFT) model. Detailed characterization procedures are provided in Text S2.

2.4. Positron annihilation lifetime (PAL) spectroscopy

Positron annihilation lifetime (PAL) spectroscopy experiments to reveal the micropore structure of ferrihydrite and hematite were carried out at the University of Science and Technology of China. The experiments were performed at room temperature using a digital PAL spectrometer (Techno AP, Japan) with a time resolution of 200 ps in FWHM. The prepared sample powder was pressed into disc-shaped pellets with a diameter of 8 mm and a thickness of ~2 mm. During PAL experiments, the positron source (^{22}NaCl, around 30 μCi, sealed by two 7.5-μm-thick Kapton foils) was sandwiched between two identical pellets. The sample-source-sample set was fixed in a vacuum chamber (vacuum better than 10^{-3} Pa) which was evacuated by a turbo molecular pump. The PAL spectra were recorded with a total count of 4 million and decomposed using the LTv9 software.

2.5. X-ray absorption near edge structure analysis

X-ray absorption near edge structure (XANES) measurements at the As K-edge of the samples were performed at the 1W1B beam line of the Beijing Synchrotron Radiation Facility (BSRF, China). To avoid photo-oxidation of As(III) on the ferrihydrite surface, all the samples to be tested were stored in the dark before collecting the As K-edge XAS spectra data. As K-edge XAS spectra were collected using fluorescence mode over the energy range of 11660–12600 eV in air atmosphere at room temperature. The corresponding monochromator energy was calibrated using As(0)

(E_0 = 11867 eV). XAS data analyses were conducted using IFFEFIT software package.

2.6. Arsenic adsorption on ferrihydrite

Arsenic adsorption experiments were carried out on a thermostatic shaker with a velocity of 200 rpm at 25 °C. To avoid photo-oxidation of As(III) on ferrihydrite surfaces, all batch experiments were performed in the dark. 3-morpholinopropanesulfonic acid (MOPS, 5 mM) and $NaNO_3$ were used to adjust the solution pH and ionic strength to 6.0 and 0.1 M, respectively. Typically, ferrihydrite (0.01 g) was added into 100 mL arsenic solution in a 150 mL Erlenmeyer flask. Initial arsenic concentrations ranged from 26.67 to 160 μM. After 24 h, the suspensions were filtered through a 0.22 μm membrane filter, and the supernatants were collected to detect residual arsenic concentrations. Actual arsenic-polluted groundwater has a wide range of As(III) and As(V) ratios. Hence, further experiments were conducted to examine the adsorption capacities of ferrihydrite for arsenic removal by setting As(III)/As(V) molar ratios to 9/1, 7/3, 5/5, 3/7, and 1/9, respectively. The experimental procedures remained the same as above batch experiments for single As(III) or As(V) adsorption, except for fixing each arsenic concentrations to the targeted As(III)/As(V) molar ratios. To investigate the arsenic adsorption on ferrihydrite at different pH, the pH values of arsenic solution were adjusted using MOPS buffer to pH values of 4.0, 6.0, 8.0, and 10.0, respectively. Three mixed arsenic solutions with As(III)/As(V) molar ratios of 10/0, 5/5, and 0/10 were selected. Initial total arsenic concentration for the three solutions was fixed as 133.3 μM, and ferrihydrite dosage was 0.1 g L^{-1}. Moreover, As(III) and As(V) adsorption kinetic behaviors on ferrihydrite samples were evaluated at pH 6.0 with an ionic strength of 0.1 M. The initial ferrihydrite dosage and arsenic concentration were set as 0.1 g L^{-1} and 133.3 μM, respectively. First, ferrihydrite (0.2 g) was added to a 2 L arsenic solution (133.3 μM). At each given interval, 10 mL suspensions were withdrawn and filtered through a 0.22 μm membrane filter. Supernatants were collected for quantification of As concentrations and speciation. All experiments were carried out in triplicates.

2.7. Arsenic desorption experiment

Prior to the desorption experiment, As(III) and As(V) solutions (100 mL) with different initial concentrations ranging from 26.7 to 400.3 μM were used to react with ferrihydrite (0.1 g L^{-1}) on a thermostatic shaker with a velocity of 200 rpm at 25 °C. After 24 h, the solids and supernatants were quickly separated through a 0.22 μm membrane filter. Supernatants were collected to measure arsenic concentrations for calculating the amount of arsenic adsorbed on ferrihydrite. The obtained solids were washed several times to remove arsenic species that were loosely associated with the ferrihydrite surface. As phosphate strongly competes with arsenic for sorption on ferrihydrite (Zhu et al., 2011), a Na_3PO_4 solution was used in this study as an eluent. First, the obtained solids were added into 100 mL of Na_3PO_4 solution (183 μmol PO_4^{3-} L^{-1}) in a 150 mL flask, which was subsequently placed on a thermostatic shaker with a velocity of 200 rpm at 25 °C. After 24 h, the arsenic concentration in solution remained constant, indicating that the arsenic adsorption-desorption reached equilibrium. The suspensions were subsequently filtered through a 0.22 μm membrane filter, and the supernatants were collected for testing the arsenic concentration. For comparison, an As desorption experiment was also conducted with hematite following the experimental procedure above. Considering that the hematite sample has a relatively low specific surface area (38.9 m^2 g^{-1}) compared to that of ferrihydrite (223.6 m^2 g^{-1}), the initial dosage concentration of hematite used in this study was 0.57 g L^{-1} to obtain a similar total surface area.

2.8. Arsenic detection

Total As (As(T)) in solution was quantified on an AFS-9700 atomic fluorescence spectrometry (AFS, Beijing Haiguang Instruments Co., China) following a previous report (Hong et al., 2018). L-ascorbic acid and thiourea were used as reductants to transform As(V) to As(III). A solution of 5% HCl-2% KBH_4 was used as carrying fluid for determining As(T) (Liu et al., 2019). The As(III) and As(V) speciation in solution were quantitatively analyzed by high-performance liquid chromatography coupled with atomic fluorescence spectrometry atomic fluorescence spectrometry (HPLC-AFS). The experimental conditions were described as follows. The As(III) and As(V) species were separated using a Hamilton PRP-X100 anion exchange column. 15 mmol L^{-1} phosphate buffer solution ($(NH_4)_2HPO_4$) at pH 6.0 was prepared as mobile phase. The reductant solution was prepared by dissolving 10.0 g KBH_4 and 1.75 g KOH in 500 mL deionized water. The detection limitation of AFS for As(T) and HPLC-AFS for As(III) and As(V) speciation was 5 μg L^{-1}.

2.9. DFT calculation

Arsenic adsorption on ferrihydrite was investigated using the plane wave based periodic DFT method as implemented in the Vienna Ab Initio Simulation Package (VASP). As ferrihydrite contains tetrahedrally and octahedrally coordinated Fe, a (001) ferrihydrite surface was therefore modeled to expose two active sites for As adsorption. The structural parameters of ferrihydrite were used according to the structural model proposed by Michel et al. (2007). H_3AsO_3 and $H_2AsO_4^-$ species were used for the calculations, because they are the predominant As(III) and As(V) species in the pH range from 3 to 7. The electron-ion interaction was described with the projector augmented wave (PAW) method (Blöchl, 1994; Kresse and Joubert, 1999). The electron exchange and correlation energies were treated within the generalized gradient approximation in the Perdew- Burke-Ernzerhof function (GGA-PBE) (Perdew et al., 1996). The plane wave basis was set to 520 eV. A 1 × 1 × 1 Gamma centered grid was used as Brillion zone K-point sampling for the structural calculations. The energy and force criterion for convergence of the electron density were set as 10^{-6} eV and 0.02 eV $Å^{-1}$, respectively.

3. Results

3.1. Arsenic adsorption on ferrihydrite

As shown in the adsorption isotherms in Fig. 1, ferrihydrite exhibited different adsorption capacities towards As(III) and As(V). The maximum As(III) adsorption capacity of ferrihydrite, fitted by the Langmuir model, was 973.2 μmol g^{-1}, which was considerably higher than that of As(V) (372.4 μmol g^{-1}) (Fig. 1a and Table S1) (Supplementary Material). Considering that the empirical Freundlich model doesn't constrain the sorption to monolayer adsorption sites compared to the Langmuir model, the As(III) and As(V) adsorption capacities of ferrihydrite were further evaluated by fitting isotherm adsorption curves using the Freundlich model (Fig. 1b). We found that the As(III) adsorption capacity (861.6 μmol g^{-1}) of ferrihydrite, obtained from the Freundlich model, was still larger than that of As(V) (349.7 μmol g^{-1}) when the equilibrium concentration of solution arsenic was ~70 μmol L^{-1} (Fig. 1b). Moreover, the isotherm adsorption of ferrihydrite for mixed As(III) and As(V) solutions with As(III)/As(V) molar ratios

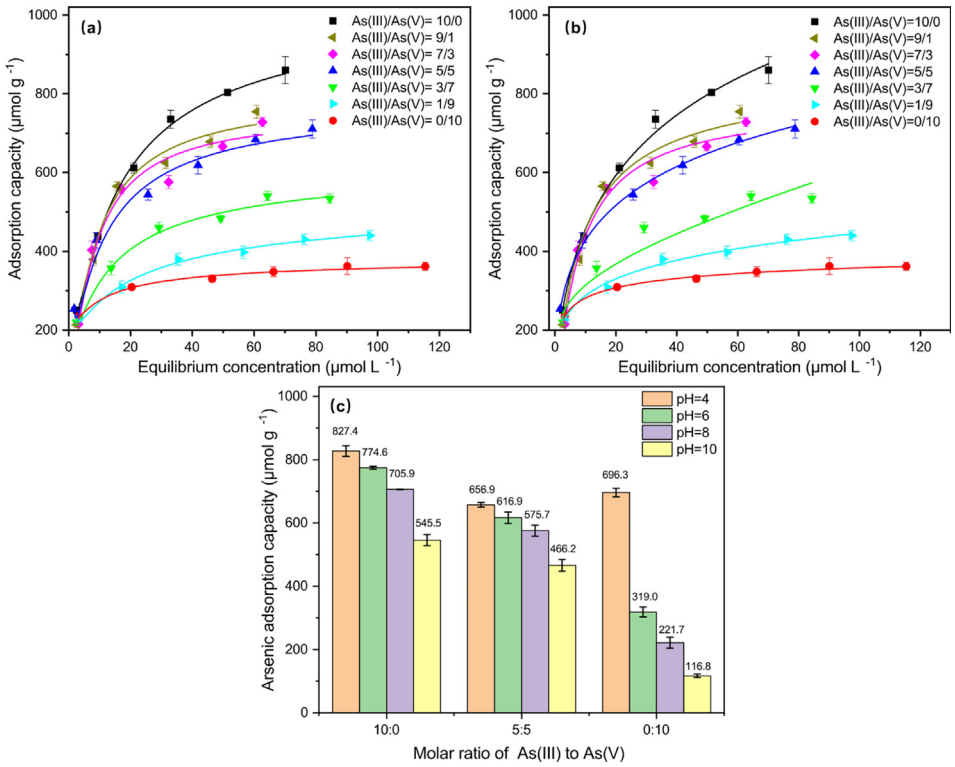

Fig. 1. Arsenic adsorption isotherms curves fitted by Langmuir (a) and Freundlich (b) models at different As(III)/As(V) molar ratios. The total arsenic adsorption capacities of ferrihydrite at different pH values under the initial As(III)/As(V) molar ratios of 10/0, 5/5, and 0/10, respectively (c): Initial total arsenic concentration was 133 μM and ferrihydrite concentration was 0.1 g L^{-1}.

of 1/9, 3/7, 5/5, 7/3, and 9/1 were also investigated (Fig. 1a and b). The corresponding results fitted by Langmuir and Freundlich models are listed in Table S1. The data reveals that increasing initial As (III)/As(V) molar ratios led to a considerable increase in maximum arsenic adsorption on ferrihydrite. When the As(III)/As(V) molar ratio increased from 0/10 to 1/9, 3/7, 5/5, 7/3, and 9/1, the maximum arsenic adsorption on ferrihydrite, fitted by Langmuir model increased from 372.4 to 466.3, 587.3, 753.3, 838.5, and 839.7 μmol g^{-1}, respectively (Table S1).

To explore the evolution of arsenic adsorption on ferrihydrite as a function of pH, the arsenic adsorption capacities of ferrihydrite at pH values of 4.0, 6.0, 8.0, and 10.0 were evaluated. As shown in Fig. 1c, an increasing pH had a negative effect on the arsenic adsorption on ferrihydrite, i.e., the total amount of arsenic adsorbed to ferrihydrite decreased with increasing solution pH from 4.0 to 10.0. Remarkably, the total amount of arsenic adsorbed to ferrihydrite with As(III)/As(V) molar ratios of 10/0 was always larger than in solutions with As(III)/As(V) molar ratios of 5/5 and 0/10 at pH values of acidic (e.g., pH 4), near neutral (e.g., pH 6 and 8), and alkaline (e.g., pH 10) conditions. These results indicated that arsenic speciation had a significant effect on the total amount of adsorbed arsenic on ferrihydrite at the same pH, and the higher the fraction of initial As(III) species was in solution, the higher the total amount of arsenic adsorbed on ferrihydrite.

3.2. The distribution of arsenic species in solution and solid

The speciation of dissolved arsenic species was examined after ferrihydrite reacted with different arsenic solutions with As(III)/As (V) molar ratios ranging from 0/10 to 1/9, 3/7, 5/5, 7/3, 9/1, and 10/0, respectively. As shown in Fig. 2a, after ferrihydrite reacted with single As(III) (As(III)/As(V) molar ratio of 10/0) at pH 6.0, the arsenic in solution occurred only as As(III) species and no As (V) was detected. The oxidation state of arsenic adsorbed on ferrihydrite after reaction with single As(III) was also investigated using As K-edge XANES spectroscopy (Fig. 2b). As_2O_3 and Na_3AsO_4 powders were used as standard reference samples. After reaction with As(III), the As K-edge XANES spectra for the reference manganese oxide sample showed a strong peak at ~11874.0 eV, which was similar to those with Na_3AsO_4, suggesting that As(III) was completely oxidized to As(V) by the Mn oxide, a strong oxidant commonly found in natural environments (Gude et al., 2017; Hou et al., 2018, 2017, 2016; Manning et al., 2002; Villalobos et al., 2014). In contrast, a strong peak in the K-edge XANES pattern was observed at ~11871.3 eV in the setup in which As(III) interacted with ferrihydrite, which was assigned to As(III) species, as evidenced by the As K-edge XANES patterns from the As_2O_3 reference sample. Moreover, As(III) and As(V) species were observed to coexist in the mixed As(III) and As(V) solutions (Fig. 2a). The residual As(III) concentration in the mixed arsenic solutions with initial As(III)/As(V) molar ratios of 1/9, 3/7, 5/5, 7/3, and 9/1 increased from 2.6 to 6.5, 16.3, 24.6, 42.1, and 49.3 μmol L^{-1}, respectively, while that for As(V) concentration decreased from 92.0 to 61.1, 55.3, 32.9, and 11.9 μmol L^{-1}, respectively.

The effect of pH on the distribution of arsenic species in solution was investigated after ferrihydrite reacted with three arsenic solutions of initial As(III)/As(V) molar ratios of 10/0, 5/5, 0/10, respectively (Fig. S1) (Supplementary Material). For single As(III) and As (V), the predominant arsenic species in solution were As(III) and As(V) at any given pH values, respectively. For the mixed arsenic solutions with an initial As(III)/As(V) molar ratio of 5/5, the residual As(III) concentrations at pH 4.0, 6.0, 8.0, and 10.0 were 16.5, 16.3, 12.3, and 19.5 μmol L^{-1}, respectively, while the concentrations for As(V) were 54.4, 55.3, 60.8, and 65.2 μmol L^{-1}, respectively.

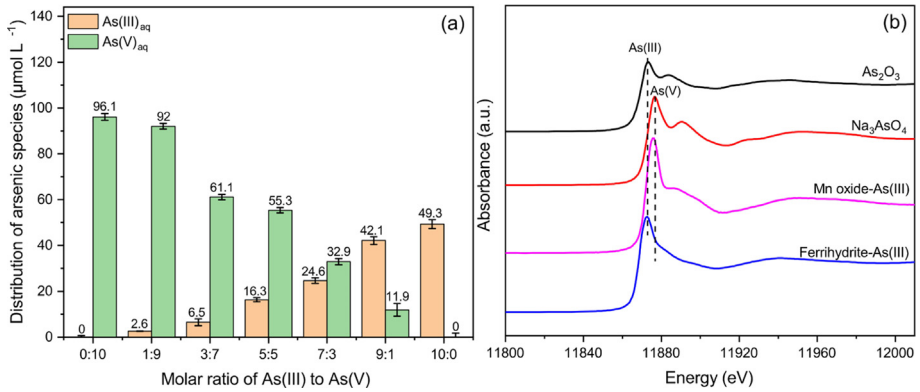

Fig. 2. The distribution of solution arsenic species after ferrihydrite reacted with arsenic solutions of As(III)/As(V) molar ratios of 0/10, 1/0, 3/7, 5/5, 7/3, 9/1, and 10/0 at pH 6.0 (a): Initial total arsenic concentration was 133 μM and ferrihydrite concentration was 0.1 g L^{-1}. Normalized As K-edge XANES in As(III) adsorbed and reference samples (b).

3.3. Structural evolution of ferrihydrite after reaction with arsenic

XRD patterns of the as-synthesized ferrihydrite exhibited two broad peaks at ~34.4° and ~62.1°, which indicated the presence of 2-line ferrihydrite (Fig. S2a). The Rietveld refinement result of XRD data revealed a particle size of 1.68 ± 0.20 nm (Fig. S3), which was close to that reported previously (Wang et al., 2016). After reaction with single As(III) and As(V), the peak position and intensity of the XRD patterns in ferrihydrite remained approximately the same compared to that of fresh ferrihydrite (Fig. S2a). No new mineral phases (e.g., ferric arsenate and scorodite) were observed in the XRD patterns. Fig. S2b illustrates the Raman spectra of ferrihydrite after reaction with As(III) and As(V). As shown in Fig. S2b, a strong band at ~710 cm^{-1} and two relatively weak bands at ~370 and ~510 cm^{-1} were observed in the fresh ferrihydrite and could be attributed to the characteristic peaks of ferrihydrite (Das and Hendry, 2011; Hanesch, 2009). After reaction with arsenic, these three characteristic peaks still appeared in the reacted ferrihydrite. Remarkably, a relatively weak peak at ~840 cm^{-1} was also observed in the ferrihydrite sample after reaction with As(V), as observed previously already (Das and Hendry, 2011; Jia et al., 2006; Muller et al., 2010). Muller et al. (2010) employed Raman spectroscopy and observed a distinct band at ~840 cm^{-1} on ferrihydrite after reaction with arsenate. Moreover, Jia et al. (2007) observed a peak at ~845 cm^{-1} that occurred in the Raman spectrum of the arsenate-ferrihydrite sorption product at pH 8. They attributed this new peak at ~845 cm^{-1} to the As—O stretching vibration of the bidentate-complexed arsenate on ferrihydrite surface. Moreover, two relatively weak peaks at ~610 and ~840 cm^{-1} appeared in the ferrihydrite sample after reaction with As(III) and were attributed to the As—O vibration mode of As(III) species adsorbed on the ferrihydrite surface (Muller et al., 2010; Sudhakar et al., 2018).

The FTIR spectra profiles of ferrihydrite before and after reaction with arsenic are shown in Fig. S4. After reaction of ferrihydrite with arsenic, some new characteristic IR peaks appeared in the range of 700–1000 cm^{-1}, which were attributed before to the characteristic peaks of As—O bond vibrations (Bhandari et al., 2011; Guan et al., 2008; Gupta et al., 2009; Jia et al., 2007; Li et al., 2020). Two IR characteristic peaks at ~791 and ~882 cm^{-1} were observed in ferrihydrite after reaction with As(III), which were attributed to the vibrations of As(III)—O in the ≡(FeO)As(III) (monodentate) and ≡$(FeO)_2$AsO (bidentate) complexes, respectively (Li et al., 2020). In addition, two IR characteristic peaks at ~809 and ~873 cm^{-1} could be observed in ferrihydrite after reaction with As(V). These two peaks were assigned to the vibrations of As(V)—O in the monodentate complex of ≡(FeO)AsO_3 and bidentate complex of ≡$(FeO)_2AsO_2$, respectively (Guan et al., 2008; Gupta et al., 2009; Li et al., 2020). The specific surface area (SSA) of ferrihydrite, obtained from the Brunauer-Emmett-Teller (BET) model, was 223.6 ± 3.0 m^2 g^{-1}, which was close to the corresponding value reported in previous studies (Eusterhues et al., 2008; Lan et al., 2018; Zhu et al., 2011). After reaction with single As(III) and As(V), the SSA of ferrihydrite changed from 223.6 ± 3.0 to 245.1 ± 7.4 and 219.5 ± 7.4 m^2 g^{-1}, respectively.

3.4. Evolution of the ferrihydrite morphology after reaction with arsenic

Fig. 3 shows the ferrihydrite morphology before and after reaction with As(V) and As(III). SEM and TEM images revealed that fresh ferrihydrite exhibited an irregular mass morphology containing aggregates of many small particles (Fig. 3a and b). After reaction with As(V) and As(III) solutions, ferrihydrite still maintained an irregular morphology consisting of many small particles (Fig. 3e, f, i, and j). Remarkably, the dispersion of ferrihydrite nano-crystallites before and after reaction with arsenic was too poor to readily observe single nanoparticles. This phenomenon was also observed in previous work (Janney et al., 2000; Wang et al., 2016). The size of ferrihydrite nano-crystallites before and after reaction with arsenic, estimated by HRTEM images (Fig. 3c, g, and k, selected particle in red circles), ranged from 2 to 6 nm, which is in agreement with previous studies (Villacís-garcía et al., 2015; Weatherill et al., 2016). The selected-area electron diffraction (SAED) patterns of fresh ferrihydrite exhibited two broad rings with the d values of 0.25 and 0.15 nm, respectively (Fig. 3d), corresponding to 2-L ferrihydrite (Janney et al., 2000). After reaction with As(V) and As(III), the SAED patterns of ferrihydrite showed no obvious changes compared to that of fresh ferrihydrite, and no new rings corresponding to new phases such as scorodite or the product of arsenic polymerization (AsO_x) were observed (Fig. 3f and l).

EDS-mapping analysis showed that arsenic species were evenly distributed on the surface of the ferrihydrite (Fig. S5). Interestingly, after carefully examining the As/Fe molar ratio in the reacted ferrihydrite, we observed that the As/Fe molar ratio in ferrihydrite after reaction with As(III) (0.087) was higher than the ratio after reaction with As(V) (0.064) under the same experimental conditions (Fig. S5). This revealed that the total arsenic content adsorbed to ferrihydrite after reaction with As(III) was higher than that after reaction with As(V).

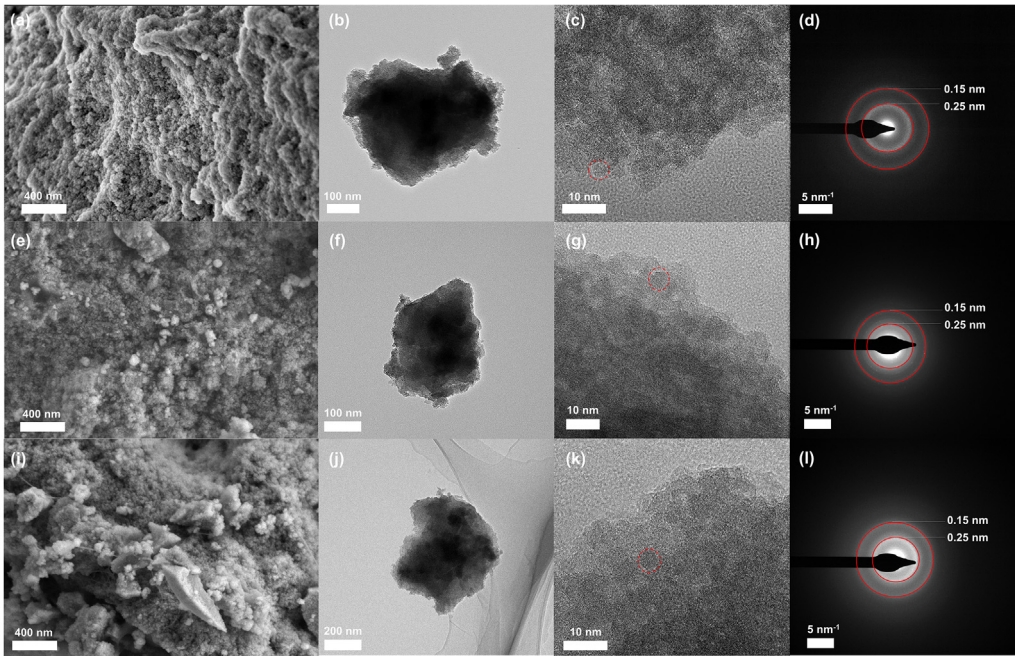

Fig. 3. SEM, TEM, HRTEM images, and SAED patterns of ferrihydrite samples before (a, b, c, and d) and after reaction with single As(V) (e, f, g, and h) and As(III) (i, j, k, and l) solutions. Initial total arsenic concentration was 133 μM and ferrihydrite concentration was 0.1 g L^{-1}.

3.5. Pore distribution analysis

The pore size distribution of ferrihydrite was characterized using N_2 adsorption and desorption isotherms. As shown in Fig. 4a, N_2 adsorption on ferrihydrite showed a rapid increase at relatively low pressures ($P/P_0 < 0.01$). This result indicated that ferrihydrite possessed a well-developed micropore structure (<2 nm). In contrast, hematite had an extremely low N_2 adsorption volume at relatively low pressures ($P/P_0 < 0.01$), suggesting that there were only very few micropores in the hematite precipitate. To accurately obtain the information on the size of the micropores, non-linear density functional theory (NLDFT) model (Cracknell et al., 1995; Suresh et al., 2019) was employed to describe the pore size distribution of ferrihydrite and hematite calculated from the adsorption isotherms. As shown in Fig. 4b, ferrihydrite exhibited a trimodal pore distribution with three narrow peaks at ~6.6, ~12.8, and ~23.0 Å. However, the pore size distributions of hematite mainly occurred at ~28.9, ~74.0, and ~221.7 Å, which were obviously larger than those of ferrihydrite.

Positron annihilation lifetime (PAL) spectroscopy is an extremely sensitive tool for detecting porous and/or vacancy structures of minerals (Gidley et al., 2006). In this study, PAL experiments were conducted for further illustrating the micropore structure of ferrihydrite. Fig. 5 shows the peak-normalized PAL spectra of ferrihydrite and hematite samples. We observed that there was a long lifetime in the PAL spectrum of hematite compared to that of ferrihydrite. This result indicated that ferrihydrite had a different surface pore structure than hematite. Based on previous studies, the PAL spectra were well decomposed into three distinct components, i.e., τ_1, τ_2, and τ_3 (Table 1). The shortest lifetime component (τ_1, 209–222 ps) was assigned to the positron annihilation in the defect-free bulk regions and tiny vacancies (Dutta et al., 2006;

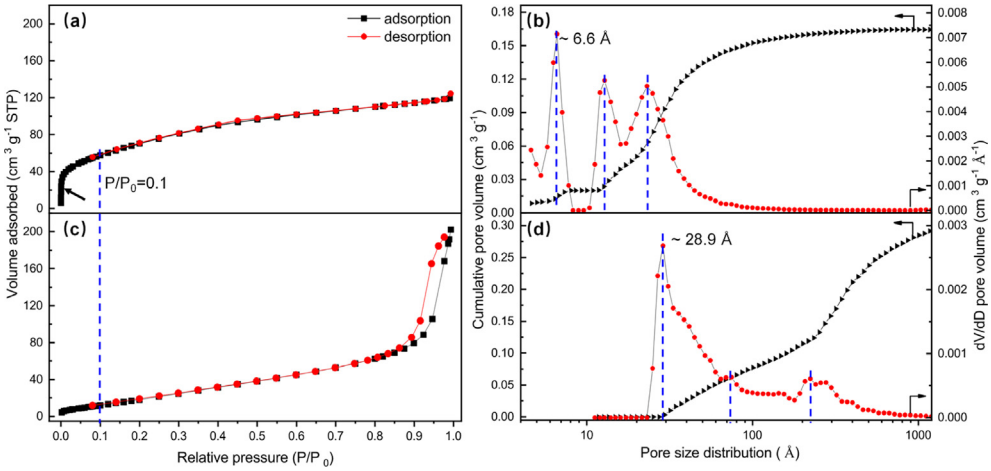

Fig. 4. N_2 adsorption/desorption isotherms, pore-size distribution, and pore-volume of ferrihydrite (a, b) and hematite (c, d). The pore-size distribution and pore-volume were calculated from the adsorption isotherms using the non-linear density functional theory (NLDFT) method.

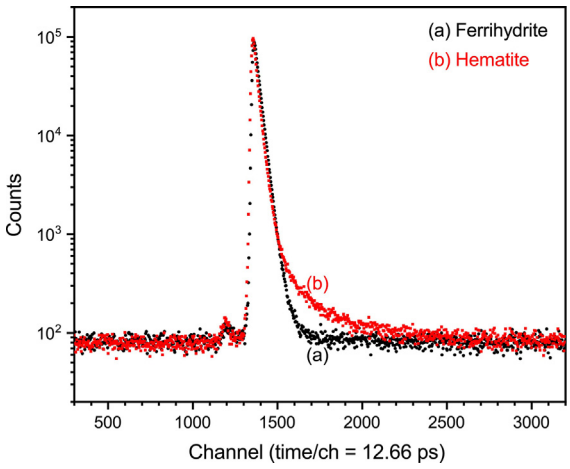

Fig. 5. Positron annihilation lifetime spectra of ferrihydrite (a) and hematite (b) samples.

Kong et al., 2011; Liu et al., 2009). The medium lifetime component (τ_2, 362–405 ps) could be attributed to the positron annihilation in large size defects, such as vacancy clusters in materials (Liu et al., 2009). The vacancy clusters usually consisted of several atom deficiencies (sometimes more than 10 atom deficiencies), and the longer the lifetime of τ_2, the larger the size of vacancy clusters. According to previous work (Nagai et al., 2003), the τ_2 lifetime at 350–400 ps corresponded to 10–20 atom vacancy clusters ($V_{10\text{-}20}$), which were large enough to form micropore-like structures in the ferrihydrite. The longest lifetime component (τ_3, longer than 1 ns) corresponded to the pick-off annihilation of ortho-positronium (o-Ps) inside large voids (unoccupied space among nanograins) in the mineral materials (Dutta et al., 2006; Liu et al., 2009). From this analysis it can be concluded that vacancy clusters as well as large voids were the two main sources that contributed to the micropore structure of ferrihydrite. Therefore, the τ_2 and τ_3 components and their corresponding intensity (I_2 and I_3) could be used to reveal their relative contributions to the micropores. As shown in Table 1, the I_2 in ferrihydrite was as high as 96.3%, which was much higher than I_3 (0.2%) in ferrihydrite. The mean void radius (R) of ferrihydrite and hematite were calculated according to the semi-empirical equation (Eq. (1)) using the *ortho*-positronium (o-Ps) lifetime (τ_3) (Zhang et al., 2010).

$$\tau_3 = \frac{1}{2}\left[1 - \frac{R}{R+\Delta R} + \frac{1}{2\pi}\sin\left(\frac{2\pi R}{R+\Delta R}\right)\right]^{-1} \quad (1)$$

where △R was the fitted empirical electron layer thickness (0.1656 nm). The calculated mean void radius (R) of ferrihydrite and hematite was 0.7934 and 0.3720 nm, respectively. As the molecular kinetic diameter of N_2 was 0.362 nm, the characterization of N_2 adsorption and desorption isotherms also could detect the large voids in the minerals.

3.6. Arsenic adsorption kinetics on ferrihydrite

Fig. 6 shows the evolution of the amount of arsenic adsorbed on ferrihydrite as a function of reaction time. As(III) adsorption on ferrihydrite was relatively fast within the initial ~5 h, while As(V) adsorption was fast within the initial first hour. To explain the process and mechanism of As(III) and As(V) adsorption on ferrihydrite, pseudo-first order and pseudo-second order models were employed to fit their corresponding adsorption kinetic data. The equations of these models are shown in Eqs. (2) and (3), respectively (Simonin, 2016; Revellame et al., 2020).

$$Q_t = Q_e(1 - e^{-k_1 t}) \quad (2)$$

$$Q_t = \frac{{Q_e}^2 k_2 t}{1 + Q_e k_2 t} \quad (3)$$

where Q_e and Q_t (μmol g^{-1}) were the amount of arsenic adsorbed on ferrihydrite at equilibrium and at a given time t (h), respectively. k_1 (h^{-1}) and k_2 (g μmol$^{-1}h^{-1}$) were the pseudo-first order and pseudo-second order rate constants, respectively.

The fitting results of As(III) and As(V) adsorption kinetics data using the pseudo-first order and pseudo-second-order models are shown in Fig. 6a, and the relevant parameters obtained are listed

Table 1
Position lifetime parameters of ferrihydrite and hematite samples.

Sample	τ_1 (ps)	τ_2 (ps)	τ_3 (ns)	I_1 (%)	I_2 (%)	I_3 (%)
Ferrihydrite	209.0	362.5	14.10	3. 5	96.3	0.2
Hematite	222.4	404.8	3.08	58.1	39.1	2.8

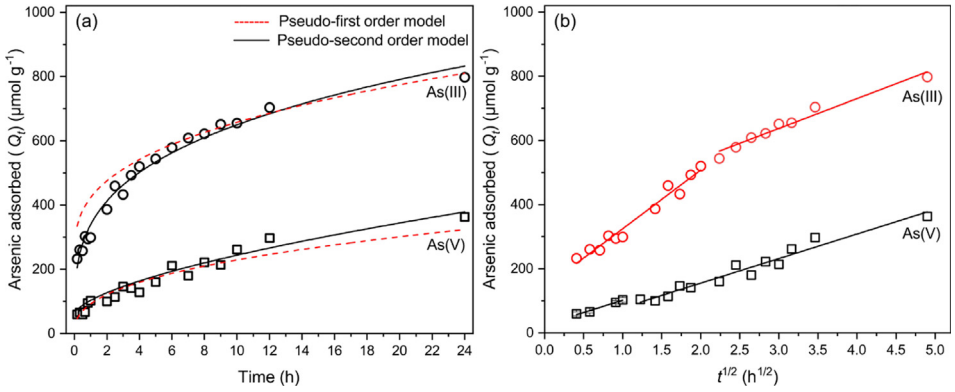

Fig. 6. Kinetics of As(III) and As(V) adsorption on ferrihydrite at pH 6.0 under room temperature. As(III) and As(V) kinetic data fitted (a) by pseudo-first-order and pseudo-second-order models and (b) by the intraparticle diffusion model, respectively. Initial As concentration was 133 μM and ferrihydrite concentration was 0.1 g L^{-1}.

in Table S2. As shown in Table S2, the coefficient values of determination (R^2) for the pseudo-first order model was slightly higher than that for the pseudo-second order model, suggesting that the pseudo-second order model was more suitable for fitting the As (III) and As(V) adsorption kinetics than the pseudo-second order model. As the intraparticle diffusion model considered adsorption processes containing a series of distinct steps, such as film diffusion (external diffusion) and pore diffusion (Maliyekkal et al., 2009), the adsorption kinetic data of As(III) and As(V) were also fitted using the intraparticle diffusion model. The equation of the intraparticle diffusion model is described in Eq. (4) (Tan and Hameed, 2017; Valderrama et al., 2008).

$$Q_t = k_p t^{0.5} + C \quad (4)$$

where k_p was the intraparticle diffusion rate constant (μmol g^{-1} $h^{-1/2}$), and C (μmol g^{-1}) was a constant indicating the thickness of the boundary layer.

Fig. 6b shows the intraparticle diffusion plot of Q_t versus $t^{1/2}$ for As(III) and As(V) adsorption on ferrihydrite, respectively. The corresponding kinetic parameters are listed in Table S3. Obviously, the plot for As(III) adsorption on ferrihydrite over the entire reaction was not linear, but could be divided into two linear sections. In general, the complete processes of adsorption comprise three steps (Ho et al., 2000; Tan and Hameed, 2017). The first step is the transport of the adsorptive from the bulk aqueous phase to the external surface of the adsorbent (external diffusion). The second step is the diffusion of the adsorptive from the external surface into the pore structure of the adsorbent (pore diffusion), while the third step is attributed to the surface reaction between the adsorptive and internal surface sites of the sorbent. The third step is very fast compared to the first and second steps, which therefore is not considered to be a rate-controlling step during the adsorption processes (Tan and Hameed, 2017). According to the analysis above, the first and second linear sections of the As(III) adsorption process were attributed to the external diffusion and pore diffusion, respectively. The fitted slope for As(III) at the first and second linear sections were 182.9 and 92.8 μmol g^{-1} $h^{-1/2}$, respectively. Moreover, we found that the fitted slope for As(V) adsorption at the first linear section (76.4 μmol g^{-1} $h^{-1/2}$) was very close to that at the second linear section (76.6 μmol g^{-1} $h^{-1/2}$). This result indicated that As(V) had obviously different adsorption behavior on ferrihydrite compared to As(III).

4. Discussion

4.1. Adsorption versus surface precipitation, incorporation, and polymerization

Adsorption is a common process for As(III) and As(V) immobilization by iron (oxyhydr)oxides (Manning et al., 1998; Onanguema et al., 2005; Raven et al., 1998; Waychunas et al., 1993). However, surface precipitation (Jia et al., 2006; Jiang et al., 2015), structural incorporation (Bolanz et al., 2013), and polymerization (Majzlan et al., 2014; Schindler et al., 2022) of arsenic were also observed to contribute to the immobilization of As(III) and As(V) under certain conditions. For example, Jia et al. (2006) provided experimental evidence for the occurrence of surface precipitation of arsenate on ferrihydrite at acidic pH of 3–5 a ratio of As/Fe of ~0.125–0.49 and a dissolved arsenic equilibrium concentration of <0.02–440 mg/L. This result suggested that the relatively low pH and high ratio of As/Fe were the two key factors inducing the surface precipitation of arsenate. Remarkably, in our study the As/Fe molar ratios in ferrihydrite after reaction with As(III) (0.087) and As(V) (0.064), determined by EDS analysis, were obviously lower than the required minimum As/Fe molar ratio (0.125) for surface precipitation on ferrihydrite (Fig. S5). In addition, the set solution pH for isotherm adsorption experiments in this study was close to neutral (pH 6.0). This may be the reason why we did not observe the formation of a ferric arsenate precipitate, as evidenced by the characterization analysis of XRD, HRTEM, and SAED (Figs. S1 and 3). In addition to this example of As surface precipitation, Bolanz et al. found that As^{5+} could enter the structure of an iron oxide, in this case hematite. However, the structural incorporation of As^{5+} into the iron oxide took place at high temperature (200 °C) within 7 days with an initial $As_2O_5/Fe(NO_3)_3$ reactant molar ratio of 0.5 (Bolanz et al., 2013). Because our experiments were performed at ambient temperature, As^{3+} or As^{5+} species did not enter into the structure of ferrihydrite - also since all adsorption experiments in this study were carried out at an initial As/Fe molar ratio far lower than 0.5. Formation of polymerized (AsO_x) polyhedra was also reported to occur in soil and sediment environments (Majzlan et al., 2014; Schindler et al., 2022). For example, Schindler and coauthors employed transmission electron microscopy (TEM) and atom probe tomography (APT) techniques to observe the polymerization of As^{3+} (AsO_x) in areas of the ferrihydrite grain where As was enriched (Schindler et al., 2022). Majzlan et al. (2014) used EXAFS analysis to demonstrate arsenic polymerization in extremely arsenic-rich acid mine wastewaters with As concentrations of up to 80,000–130,000 mg L^{-1} and a pH value close to 0. These results suggested that formation of polymerized As^{3+} polyhedra need extreme conditions such as strong acid and high arsenic concentration. In our study, polymerized As^{3+} polyhedra such as arsenolite (As_2O_3) did consequently not occur in the ferrihydrite sample after reaction with As(III), as evidenced by the SAED analysis. Moreover, we also observed that the FTIR spectrum of As_2O_3 is different from that of As(III) adsorbed on ferrihydrite (Figs. S4 and S6). This suggests that the formation of polymerized As^{3+} polyhedra was not responsible for promoting As(III) immobilization by ferrihydrite.

4.2. Effect of specific surface area, phase structure, and particle size

The specific surface area (SSA) is an essential parameter determining the extent of arsenic adsorption on iron (oxyhydr)oxides. In this study, compared to fresh ferrihydrite, the surface area of samples after reaction with As(III) increased by ~9.6%, while that with As(V) decreased by ~1.6%. To illustrate whether the higher As(III) adsorption on ferrihydrite was attributed to the change of SSA, the maximum amounts of arsenic adsorbed on ferrihydrite per unit surface area at pH 6.0 for single As(III) and As(V) immobilization were calculated. The calculated maximum adsorption amounts on ferrihydrite per unit surface area for single As(III) was 3.7 μmol m^{-2}, which was still higher than that for single As(V) (1.7 μmol m^{-2}), suggesting the surface areas was not the key factor controlling the arsenic adsorption performance of ferrihydrite.

The type of iron (oxyhydr)oxides also affects the arsenic adsorption (Farquhar et al., 2002; Gim et al., 2007). Previous studies showed that the transformation rate of ferrihydrite to well-crystalline iron (oxyhydr)oxides was controlled by pH and temperature (Das et al., 2011b). XRD and Raman analysis revealed that the structure of ferrihydrite after reaction with As(III) and As(V) remained stable, and no new mineral phases such as hematite or goethite were generated. This observation also was supported by SAED analysis, i.e., new diffraction rings corresponding to hematite or goethite in our ferrihydrite sample after reaction with As(III) and As(V) did not appear. Therefore, our observations could be explained as follows. The rates of ferrihydrite transformation to more crystalline minerals ranged from 2.05×10^{-5} to 7.37×10^{-5} h^{-1} at pH 2–7 in pure suspension systems (Das et al., 2011b), suggesting that the kinetic rates of crystallization

of ferrihydrite are very slow. Moreover, the adsorbed arsenic could even have retarded the dissolution and/or transformation of ferrihydrite (Das et al., 2011a). Therefore, the transformation of ferrihydrite was too slow to affect the As(III) and As(V) immobilization in this study. The particle size was also found to influence the interfacial reactivity of ferrihydrite (Wang et al., 2016). However, HRTEM images revealed that the morphology and particle size of ferrihydrite did not change after reaction with As(III) and As(V) compared to that of fresh ferrihydrite. Therefore, changes of morphology and/or particle size could be ruled out as main contributors to the high As(III) immobilization.

4.3. Effect of arsenic species on As(III) immobilization

Arsenic species analysis showed that As(III) and As(V) were the predominant arsenic species in solution after ferrihydrite reacted with As(III) and As(V), respectively (Fig. 2a). Moreover, XANES analysis revealed that the adsorbed arsenic species on the ferrihydrite after reaction with As(III) mainly existed in the form of As(III), rather than As(V) (Fig. 2b). This result combined with solution arsenic species analysis confirmed that ferrihydrite did not oxidize As(III) to As(V). These observations undoubtedly ruled out the possibility that a change of As(III) species contributed to the relatively large As(III) adsorption on ferrihydrite. The residual As(III)/As(V) molar ratios in the mixed As(III) and As(V) solutions were also carefully examined. Interestingly, the calculated residual As(III)/As(V) molar ratios in the mixed arsenic solutions with initial As (III)/As(V) molar ratios of 1/9, 3/7, 5/5, 7/3, and 9/1 were 0.028, 0.11, 0.29, 0.75, 3.54, respectively, which were obviously lower than their corresponding initial As(III)/As(V) molar ratios, suggesting that ferrihydrite was more prone to adsorb As(III) in the mixed arsenic solution at pH 6.0. We also calculated the residual As(III)/As (V) molar ratios in the 5/5 As(III) and As(V) mixed solution at pH 4.0, 6.0, 8.0, and 10.0. The residual As(III)/As(V) molar ratio in the 5/5 As(III) and As(V) mixed solution at pH 4.0 (0.32), 6.0 (0.29), 8.0 (0.28), and 10.0 (0.32) were lower than the initial As(III)/As (V) molar ratio of 5/5. This result further demonstrated that As (III) preferably adsorbed on ferrihydrite compared to As(V) at a pH range of 4–10.

4.4. Adsorption reaction energies of arsenic on ferrihydrite surface

The ferrihydrite structure was found to consist of tetrahedrally and octahedrally coordinated iron atoms (Michel et al., 2007), while the tetrahedrally coordinated iron atom sites in ferrihydrite are commonly unstable (Maillot et al., 2011), which made it hard to experimentally observe the adsorption behavior of arsenic to the tetrahedrally coordinated iron atom sites. However, DFT calculation is an available approach to theoretically investigating the difference in arsenic adsorption on the tetrahedrally and octahedrally coordinated iron atom sites. We therefore employed DFT calculations to investigate the adsorption reaction energies of As(III) and As(V) at different Fe sites of ferrihydrite to illustrate whether As(III) and As(V) species have different adsorption behaviors on the tetrahedral and octahedral Fe sites. FTIR analysis revealed that monodentate and bidentate complexes simultaneously existed in ferrihydrite after reaction with As(III) and As(V) (Fig. S4). We calculated a bidentate adsorption model because the configuration of bidentate complexes was reported to be more stable than that of monodentate complexes (Adra et al., 2016). Fig. 7 and S7 illustrate the two adsorption sites for arsenic adsorption on the supercell of ferrihydrite. The calculation formula for adsorption reaction energy (E_{ads}) was described as follows:

$$E_{ads} = E_{slab+arsenic} - E_{slab} - E_{arsenic}$$

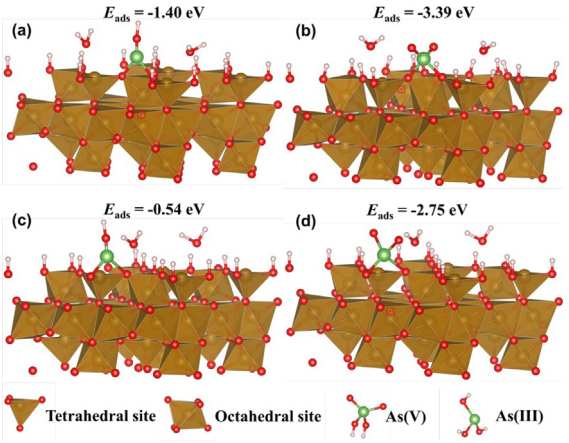

Fig. 7. Constructed supercell of ferrihydrite for As(III) (left) (a, c) and As(V) (right) (b, d) adsorption at octahedral and tetrahedral sites, respectively: red for oxygen, white for hydrogen, green for arsenic, and grey for iron. (For interpretation of the references to color in this figure legend, the reader is referred to the web version of this article.)

where $E_{slab+arseic}$ is the total energy of the supercell with arsenic, and E_{slab} and $E_{arsenic}$ represent the energy of the supercell and adsorbed arsenic.

When As(III) species adsorbed onto the octahedral Fe site (Fig. 7a), its E_{ads} was −1.40 eV, indicating that As(III) adsorbed on ferrihydrite was thermodynamically favorable, while for As(V) species, its E_{ads} at octahedral Fe site significantly decreased to −3.39 eV. This result indicated that As(V) was more readily immobilized than As(III) on the surface octahedral Fe sites of ferrihydrite. Remarkably, the adsorption reaction energy of As(V) (−2.75 eV) on the tetrahedral Fe site was still lower than that of As(III) (−0.54 eV). The high adsorption reaction energy of As(III) compared to that of As(V) means that surface adsorption sites of ferrihydrite were prone to bind As(V), rather than As(III), which was in obvious conflict with our batch adsorption experiment results (Fig. 1). Based on above analysis, except for surface adsorption sites for As(III) immobilization, we speculated that ferrihydrite may exist some adsorption sites (e.g., micropores) available only by As (III).

4.5. Effect of micropores and oxyanion arsenic size on arsenic immobilization

In general, the sites on the surface and in micropores of (oxyhydr)oxides are most likely the predominant factor controlling the immobilization of arsenic. The sites on the surface can be directly accessed by ions, while those ions with relatively small size can favorably enter the pores of minerals (Dai et al., 2016; Yang et al., 2017). N_2 adsorption and desorption curves analysis revealed that ferrihydrite had a well-developed micropore structure (Fig. 4) suggesting that ferrihydrite had a high abundance of micropore adsorption sites available for arsenic immobilization. The pore size distribution analysis demonstrated that also the well-crystalline hematite had a few micropores, and the signals of τ_2 and τ_3 components were also present in the hematite sample (Table 1). Obviously, some micropore structure still existed in hematite, indicating that PAL analysis was more sensitive to the micropore characterization than the traditional characterization of N_2 adsorption and desorption isotherms. The intensity of the τ_3 component in hematite was 2.8%, suggesting that there was relatively less pores generated from unoccupied space among hematite nanograins. Moreover, HRTEM images showed clear

aggregation of nanocrystallites in ferrihydrite (Fig. 3a and b), which was detrimental to the generation of pore spaces between ferrihydrite nanocrystallites. This explains why we observed a relatively low intensity of τ_3 in the PAL spectrum of ferrihydrite (Table 1). In this study, we provided PAL evidence for a vacancy cluster-like micropore structure in ferrihydrite, which had a dominant contribution to the formation of micropores, as evidenced by the strong intensity of the τ_2 component in ferrihydrite (96.3%) (Table 1). Previous literature had reported that minerals with low crystallinity could possess a high abundance of vacancy defects (e.g., oxygen vacancy) (Hou et al., 2014, 2013). Therefore, the high concentration of large defects (e.g., vacancy clusters) in ferrihydrite could be better explained by its poorly-crystallite structure.

Of course it has to be evaluated whether the radius of hydrated arsenic ions match well with the micropore size of ferrihydrite, otherwise, arsenic ions could not sufficiently utilize the micropore adsorption sites of ferrihydrite. In general, the radius of ions is affected by their chemical valence state. According to the Shannon's ionic radius Table, the ion radius of As^{5+} and As^{3+} are different (Shannon and Prewitt, 1969). The reported ion radius of As^{5+} was 0.335 or 0.46 Å, which was smaller than that of As^{3+} (0.58 Å) (Shannon and Prewitt, 1969). However, it should be noted that arsenic mainly exists in the form oxyanions (e.g., $H_3As^{3+}O_3$, $HAs^{5+}O_4^{2-}$, and $H_2As^{5+}O_4^-$) in natural environments, but not as cationic As^{5+} and As^{3+} species. The oxyanion of As(V) is a charged oxygen anion (e.g., $H_2AsO_4^-$ and $HAsO_4^{2-}$) that readily combines with water molecules to exhibit a large hydrated ionic radius. In contrast, at neutral pH, the oxyanion of As(III) is a neutral molecule (H_3AsO_3) that has weaker interactions with water molecules, thus showing a smaller hydrated ionic radius. Unfortunately, it was difficult to find original data for the hydrated ionic radius of As(III) in the literature, therefore we could not directly compare the sizes between As(III) and As(V) ions. Some studies reported that the diffusion coefficients (D) of ions were closely related to their hydrated ions sizes (Takahashi et al., 2011). The size (diameter, d, Å) of the arsenic species can be calculated according to the Stokes-Einstein equation (Eq. (5)) (Takahashi et al., 2011).

$$d = k_B T / 3\pi\mu D \quad (5)$$

where k_B and T represent Boltzmann constant (J K^{-1}) and absolute temperature (K), respectively. μ is the viscosity of the medium (Pa·s). In this study, we mainly focused on H_3AsO_3 and $H_2AsO_4^-$ species because they were the predominant As(III) and As(V) species at pH 6.0 (the pH value used in our batch experiments), respectively. Leaist, (2007) and Takahashi et al. (2011) reported that the corresponding D values of H_3AsO_3 and $H_2AsO_4^-$ were 11.6 × 10^{-6} and 8.3 × 10^{-6} cm^2 s^{-1}, respectively. The calculated d value of As(V) (5.90 Å) was obviously larger than that of As(III) (4.22 Å). This result indicated that the relatively small size of As(III) leads to a higher probability than As(V) for entering the small micropore sites of ferrihydrite.

4.6. The underlying contribution of micropores adsorption sites to As (III) immobilization

We detected relatively few micropores in hematite compared to ferrihydrite. To illustrate the importance of micropore adsorption sites for arsenic immobilization, the maximum adsorption amount of As(III) and As(V) on hematite was compared (Fig. S8). The maximum As(III) adsorption (51.2 μmol g^{-1}) on hematite was lower than that of As(V) adsorption (65.3 μmol g^{-1}), which was clearly different from the data obtained for ferrihydrite. The ferrihydrite had an overall higher As adsorption performance than hematite, which may be attributed to its larger surface area. As there were few micropores in hematite, the relatively high amount of As(V) adsorption on hematite was attributed to the strong adsorption affinity of As(V) on the surface sites of hematite relative to that of As(III), as evidenced by the result of DFT calculations.

To confirm whether the micropore adsorption sites participated in As(III) immobilization, As(III) and As(V) adsorption kinetic behaviors on ferrihydrite were investigated. In this study, pseudo-first order and pseudo-second order models were firstly used to fit the As(III) and As(V) adsorption kinetic data (Fig. 3a and b). Although the pseudo-second order model could be well used to describe the reaction kinetic behavior of As(III) and As(V) on ferrihydrite (Table S2), the application of pseudo-second-order model was limited, since it considered that adsorption was a single and one-step binding process, which did not distinguish the rate-limiting steps such as external diffusion and pore diffusion (Simonin, 2016). Therefore, we subsequently employed the intraparticle diffusion model to illustrate the rate-limiting steps controlling the entire reaction. The plot of Q_t versus reaction time t for As(III) adsorption showed non-linear curve, indicating that a multiple rate-limiting process controlled the overall adsorption rate (Fig. 3c). In general, external diffusion controlled the rate of adsorption only in the initial period (e.g., 0–5 h), while pore diffusion played a vital role in determining the overall adsorption rate. The relatively small slope for As(III) at second linear section (92.8 μmol g^{-1} $h^{-1/2}$) compared to that at first linear sections (182.9 μmol g^{-1} $h^{-1/2}$) meant that pore diffusion was the rate-limiting step controlling the As(III) adsorption on ferrihydrite. Moreover, we found that the slope for As(V) adsorption at second linear section (76.6 μmol g^{-1} $h^{-1/2}$) was similar to that at first linear section (76.4 μmol g^{-1} $h^{-1/2}$) (Table S3), suggesting that the plot of Q_t versus reaction time t for As(V) adsorption also could be fitted by a single straight line. According to a previous report, if the plot of Q_t versus reaction time t could be fitted by a single linear, the intraparticle diffusion (pore diffusion) was the rate-limiting step (Qiu et al., 2009). Therefore, pore diffusion was the rate-limiting step for As(V) adsorption on ferrihydrite. Remarkably, the pore diffusion rate constant of As(III) (92.8 μmol g^{-1} $h^{-1/2}$) was higher than that of As(V) (76.6 μmol g^{-1} $h^{-1/2}$). The higher pore diffusion rate constant of As(III) compared to that of As(V) indicated that the oxyanion of As(III) with a relatively small size could sufficiently utilize the micropore sites for adsorption and consequently for immobilization.

The As(III) kinetic sorption data was also fitted using the first order reaction kinetic model (Fig. 8a). Interestingly, the plot of ln (C_o/C) versus time t for As(III) adsorption on ferrihydrite was found to be divided into two linear sections. According to the result of intraparticle diffusion model analysis, these two linear sections for As(III) adsorption could be explained as follows. The first stage (0–5 h) was a rapid adsorption process that corresponded to the external diffusion step, i.e., transform of As(III) from aqueous bulk to the surface sites of ferrihydrite. In this case, the reaction kinetic constant (k_{ads}) of As(III) was as high as 0.0723 h^{-1} (Table S4). As the reaction proceeded, As(III) started to utilize the pore adsorption sites due to a gradual decrease in the surface adsorption sites. In this case, the reaction rate was controlled by the pore diffusion step. The As(III) reaction kinetic constant (0.0182 h^{-1}) at the second stage (5–24 h) was therefore lower than that at the initial stage. Due to the relatively large size of the oxyanion of As(V), the probability of utilization of micropores for As(V) adsorption became less, as evidenced by its low pore diffusion rate constant of As(V). Therefore, external diffusion was a predominant behavior observed in As(V) adsorption on ferrihydrite. This explained why the reaction kinetic constants for As(V) adsorption in the first and second linear sections showed no obvious differences.

In principle, arsenic adsorbed in the micropore sites may desorb slower than that adsorbed on the surface sites due to the limiting diffusion rate. Therefore, the desorption behavior of arsenic on ferrihydrite was examined to further explain the role of micropore

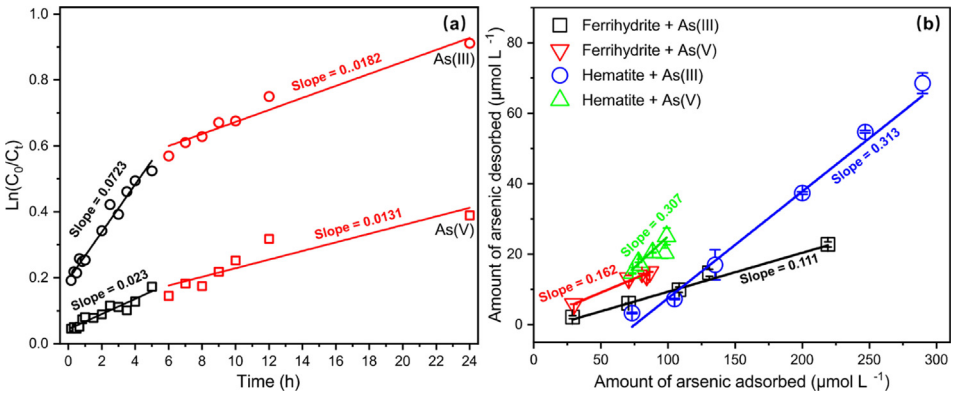

Fig. 8. The first-order reaction kinetic fitting of arsenic adsorption kinetics on ferrihydrite within first (0–5 h, black color) and second (5–24 h, red color) stages (a), and the curves of arsenic desorption concentration versus the arsenic adsorbed concentration at pH 6.0 (b). C_o and C_t (μmol L^{-1}) were the As concentration at initial and given time *t*. (For interpretation of the references to color in this figure legend, the reader is referred to the web version of this article.)

sites in As(III) adsorption. For comparison, arsenic desorption behavior on hematite was also evaluated. Fig. 8b illustrates the amount of desorbed arsenic versus the amount of adsorbed arsenic on ferrihydrite and hematite. The amount of arsenic desorbed from the two iron (oxyhydr)oxides exhibited a better linear relationship with the adsorption amount. The slope could be used as the index to reflect the mobility of the adsorbed arsenic or the desorption degree of arsenic adsorbed on iron (oxyhydr)oxides. The larger the slope, the easier desorption of any arsenic adsorbed. For hematite, the slope for As(III) (0.307) was very close to that of As(V) (0.313), indicating that As(III) and As(V) had the same desorption behavior when they were adsorbed on the surface sites of hematite. Interestingly, for ferrihydrite the desorption behavior of As (III) was different from that of As(V), i.e., the slope for As(V) (0.162) was larger than that for As(III) (0.111), indicating that As (III) was more difficult to desorb from ferrihydrite than As(V). This clearly demonstrated that micropore sites are as important as surface sites in ferrihydrite with respect to As(III) adsorption, thus considerably enhancing As(III) immobilization.

A previous study employing APT 2-D distribution maps revealed the existence of As(III) accumulation in mesopores (diameters varying from 4 to 20 nm) of the environmental ferrihydrite samples from a smelter-impacted soil (Schindler et al., 2022). Our pore-size distribution analysis (Fig. 4) revealed that ferrihydrite sample also contained mesopores that could participate in the arsenic immobilization. It should be noted that the size of mesopores in ferrihydrite was far larger than those of the oxyanions of As(III) and As(V), indicating that mesopore sites not only could be directly utilized for As(III) adsorption, but they also could contribute to As(V) immobilization. Therefore, compared to micropore sites, the presence of mesopores in ferrihydrite was not the primary factor that resulted in the different adsorption capacities of ferrihydrite towards As(III) and As(V). In this study, we provided experimental evidence revealing the important contribution of micropore sites in promoting As(III) immobilization. To sum up, ferrihydrite has a high abundance of micropore sites, which inadvertently resulted in obviously different adsorption and immobilization of As(III) and As(V). A schematic diagram of the difference in adsorption behavior between As(III) and As(V) on ferrihydrite particles is shown in Fig. 9. The micropore sites in ferrihydrite as well as the size and surface charge of arsenic ions together determine the difference in adsorption behavior of As(III) versus As (V).

Ferrihydrite is ubiquitous in soils and sediments and plays an essential role in controlling arsenic migration in the environment. In the past, it was widely accepted that As(III) had relatively poor affinity to iron oxides compared to As(V), therefore showing strong migration in natural environments. We have now combined both theoretical and experimental evidence to confirm that As(III), rather than As(V), exhibits a strong affinity to ferrihydrite. This phenomenon is clearly different from previous knowledge. The main reason is that in the past, the focus was not on the contribu-

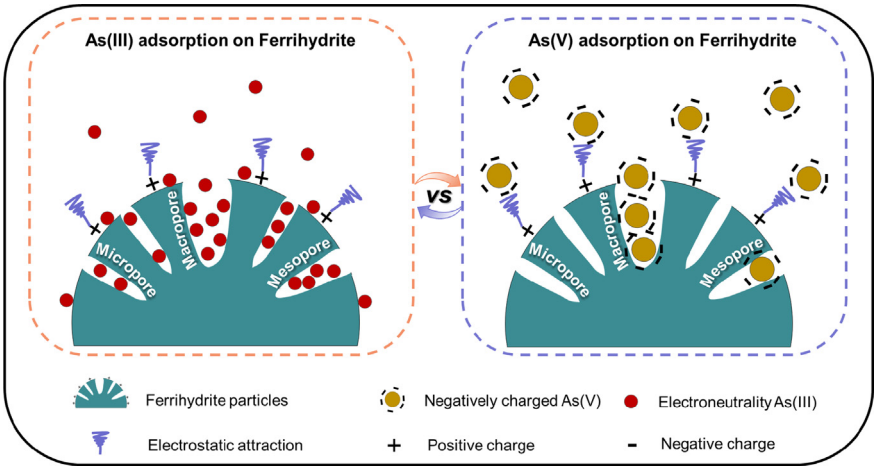

Fig. 9. Schematic illustration of the different adsorption behavior of As(III) and As(V) on ferrihydrite.

tion of micropore sites for arsenic adsorption. In addition, the differences in ion size and charge behavior between As(III) and As(V) had been considered to a lesser extent before in the literature. Although the ion radius of As^{5+} is smaller than that of As^{3+}, the hydrated ionic radius of the oxyanion of As(V) is larger than that of the oxyanion of As(III). Therefore, these two reasons together lead to an obviously different adsorption behavior of As(III) and As(V) on ferrihydrite.

5. Conclusions

In summary, the adsorption capacities of ferrihydrite for As(III) and As(V) immobilization were evaluated using batch adsorption experiments at pH 6.0. The adsorption experiments revealed that As(III) adsorption on ferrihydrite was obviously larger than that of As(V). The PAL and pore size distribution analysis confirmed that poorly-crystalline ferrihydrite had abundant vacancy cluster-like micropores that provided additional adsorption sites only available to the oxyanion of As(III) because its size matched well with that of the micropores in ferrihydrite. Although the binding of As(III) on ferrihydrite is weaker than that of As(V), the number of available adsorption sites for As(III) is clearly more than that for As(V), thereby promoting As(III) immobilization. The findings of this work provide a novel insight into the understanding of the migration risk of arsenic species in natural environments, which also aids in developing more targeted strategies to control arsenic pollution.

Declaration of Competing Interest

The authors declare that they have no known competing financial interests or personal relationships that could have appeared to influence the work reported in this paper.

Acknowledgments

This work was supported by National Natural Science Foundation of China (41977022, 42277015, 41471407), Knowledge Innovation Program of Wuhan-Shuguang Project (2022020801020231), and the Fundamental Research Funds for the Central Universities (2662022YJ017, 2662020ZHPY003). We thank Prof. Yuanzhi Li at Wuhan University of Technology for his help in DFT calculations, and Dr. Jilin Bai at Center for Materials Research and Analysis (Wuhan University of Technology) for her help in TEM-EDS mapping analysis, Beijing Synchrotron Radiation Facility (BSRF), China for XAS measurement at Beamline 1W1B. We also highly appreciated three anonymous reviewers and associate editor prof. Mario Villalobos for their constructive comments to improve the quality of this article.

Appendix A. Supplementary material

The details of sample preparation and characterization (Text S1 and S2), fitting parameters of adsorption isotherms (Tables S1, S2, and S3) and adsorption kinetics (Table S4), the distribution of solution arsenic species (Fig. S1), XRD patterns (Fig. S2a), Raman spectra (Fig. S2b), Rietveld refinement of XRD patterns (Fig. S3), FTIR spectra (Figs. S4 and S6), TEM-EDS mapping (Fig. S5), schematic illustration of the active sites of tetrahedral and octahedral Fe atoms existed in ferrihydrite slab (Fig. S7) and adsorption isotherms of hematite (Fig. S8) are available online. Supplementary material to this article can be found online at https://doi.org/10.1016/j.gca.2023.03.007.

References

Adra, A., Morin, G., Ona-nguema, G., Brest, J., 2016. Arsenate and arsenite adsorption onto Al-containing ferrihydrites. Implications for arsenic immobilization after neutralization of acid mine drainage. Appl. Geochem. 64, 2–9.
Bhandari, N., Reeder, R.J., Strongin, D.R., 2011. Photoinduced oxidation of arsenite to arsenate on ferrihydrite. Environ. Sci. Technol. 45, 2783–2789.
Blöchl, P.E., 1994. Projector augmented-wave method. Phys. Rev. B 50, 17953.
Boland, D.D., Collins, R.N., Payne, T.E., Waite, T.D., 2011. Effect of amorphous Fe(III) oxide transformation on the Fe(II)-mediated reduction of U(VI). Environ. Sci. Technol. 45, 1327–1333.
Bolanz, R.M., Wierzbicka-Wieczorek, M., Aplovičova, M.C., Uhlík, P., Göttlicher, J., Majzlan, J., Steininger, R., 2013. Structural incorporation of As^{5+} into hematite. Environ. Sci. Technol. 47, 9140–9147.
Bose, P., Sharma, A., 2002. Role of iron in controlling speciation and mobilization of arsenic in subsurface environment. Wat. Res. 36, 4916–4926.
Bylaska, E.J., Catalano, G., Mergelsberg, S.T., Saslow, S.A., Qafoku, O., Prange, M.P., Ilton, E.S., 2019. Association of defects and zinc in hematite. Environ. Sci. Technol. 53, 13687–13694.
Chang, F., Qu, J., Liu, R., 2010. Practical performance and its efficiency of arsenic removal from groundwater using Fe-Mn binary oxide. J. Environ. Sci. 22, 1–6.
Cornell, R.M., Schwertmann, U., 2003. The iron oxides: Structure, Properties, Reactions, Occurences and Uses. WILEY-VCH Verlag GmbH & Co. KGaA, Weinheim, pp. 1–7.
Cracknell, R.F., Gubbins, K.E., Maddox, M., Nicholson, D., 1995. Modeling fluid behavior in well-characterized porous materials. Acc. Chem. Res. 28, 281–288.
Dai, M., Xia, L., Song, S., Peng, C., Lopez-Valdivieso, A., 2016. Adsorption of As(V) inside the pores of porous hematite in water. J. Hazard. Mater. 307, 312–317.
Das, S., Hendry, M.J., 2011. Application of Raman spectroscopy to identify iron minerals commonly found in mine wastes. Chem. Geol. 290, 101–108.
Das, S., Hendry, M.J., Essilfie-Dughan, J., 2011a. Effects of adsorbed arsenate on the rate of transformation of 2-line ferrihydrite at pH 10. Environ. Sci. Technol. 45, 5557–5563.
Das, S., Hendry, M.J.I.M., Essilfie-dughan, J., 2011b. Transformation of two-line ferrihydrite to goethite and hematite as a function of pH and temperature. Environ. Sci. Technol. 45, 268–275.
Deschamps, E., Ciminelli, V.S.T., Höll, W.H., 2005. Removal of As(III) and As(V) from water using a natural Fe and Mn enriched sample. Wat. Res. 39, 5212–5220.
Dixit, S., Hering, J.G., 2003. Comparison of arsenic(V) and arsenic(III) sorption onto iron oxide minerals: Implications for arsenic mobility. Environ. Sci. Technol. 37, 4182–4189.
Dutta, S., Chattopadhyay, S., Jana, D., Banerjee, A., Manik, S., Pradhan, S.K., Sutradhar, M., Sarkar, A., 2006. Annealing effect on nano-ZnO powder studied from positron lifetime and optical absorption spectroscopy. J. Appl. Phys. 100, 114328.
Dzade, N.Y., De Leeuw, N.H., 2018. Density functional theory characterization of the structures of H_3AsO_3 and H_3AsO_4 adsorption complexes on ferrihydrite. Environ. Sci. Proc. Imp. 20, 977–987.
Eusterhues, K., Wagner, F., Hausler, W., Hanzlik, M., Knicker, H., Totsche, K., Kogel-Knabner, I., Schwertmann, U., 2008. Characterization of ferrihydrite-soil organic matter coprecipitates by X-ray diffraction and Mössbauer spectroscopy. Environ. Sci. Technol. 42, 7891–7897.
Farquhar, M., John, C., Livens, F., Vaughan, D., 2002. Mechanisms of arsenic uptake from aqueous solution by interaction with goethite, lepidocrocite, mackinawite, and pyrite: An X-ray absorption spectroscopy study. Environ. Sci. Technol. 36, 1757–1762.
Fritzsche, A., Rennert, T., Totsche, K.U., 2011. Arsenic strongly associates with ferrihydrite colloids formed in a soil effluent. Environ. Pollut. 159, 1398–1405.
Gidley, D.W., Peng, H.-G., Vallery, R.S., 2006. Positron annihilation as a method to characterize porous materials. Annu. Rev. Mater. Res. 36, 49–79.
Gim, J., Pablo, J.D., Rovira, M., Duro, L., 2007. Arsenic sorption onto natural hematite, magnetite, and goethite. Environ. Sci. Technol. 141, 575–580.
Grafe, M., Eick, M.J., Grossl, P.R., Saunders, A.M., 2002. Adsorption of arsenate and arsenite on ferrihydrite in the presence and absence of dissolved organic carbon. J. Environ. Qual. 31, 1115–1123.
Guan, X., Wang, J., Chusuei, C.C., 2008. Removal of arsenic from water using granular ferric hydroxide: Macroscopic and microscopic studies. J. Hazard. Mater. 156, 178–185.
Gude, J.C.J., Rietveld, L.C., Halem, D.V., 2017. As(III) oxidation by MnO_2 during groundwater treatment. Wat. Res. 111, 41–51.
Guo, H., Stu, D., Berner, Z., 2007. Removal of arsenic from aqueous solution by natural siderite and hematite. Appl. Geochem. 22, 1039–1051.
Gupta, A., Chauhan, V.S., Sankararamakrishnan, N., 2009. Preparation and evaluation of iron-chitosan composites for removal of As(III) and As(V) from arsenic contaminated real life groundwater. Wat. Res. 43, 3862–3870.
Hanesch, M., 2009. Raman spectroscopy of iron oxides and (oxy)hydroxides at low laser power and possible applications in environmental magnetic studies. Geophys. J. Int. 177, 941–948.
Ho, Y.S., Ng, J.C.Y., McKay, G., 2000. Kinetics of pollutant sorption by biosorbents: Review. Sep. Purif. Methods 29, 189–232.
Hong, J., Liu, L., Luo, Y., Tan, W., Qiu, G., Liu, F., 2018. Photochemical oxidation and dissolution of arsenopyrite in acidic solutions. Geochim. Cosmochim. Acta 239, 173–185.
Hou, J., Li, Y., Liu, L., Ren, L., Zhao, X., 2013. Effect of giant oxygen vacancy defects on the catalytic oxidation of OMS-2 nanorods. J. Mater. Chem. A 1, 6736–6741.

Hou, J., Li, Y., Mao, M., Ren, L., Zhao, X., 2014. Tremendous effect of the morphology of birnessite-type manganese oxide nanostructures on catalytic activity. ACS Appl. Mater. Interfaces 6, 14981–14987.
Hou, J., Luo, J., Hu, Z., Li, Y., Mao, M., Song, S., Liao, Q., Li, Q., 2016. Tremendous effect of oxygen vacancy defects on the oxidation of arsenite to arsenate on cryptomelane-type manganese oxide. Chem. Eng. J. 306, 597–606.
Hou, J., Xiang, Y., Zheng, D., Li, Y., Xue, S., Wu, C., Hartley, W., Tan, W., 2017. Morphology-dependent enhancement of arsenite oxidation to arsenate on birnessite-type manganese oxide. Chem. Eng. J. 327, 235–243.
Hou, J., Sha, Z., Hartley, W., Tan, W., Wang, M., Xiong, J., Li, Y., Ke, Y., Long, Y., Xue, S., 2018. Enhanced oxidation of arsenite to arsenate using tunable K^+ concentration in the OMS-2 tunnel. Environ. Pollut. 238, 524–531.
Huang, J., Voegelin, A., Pombo, S.A., Lazzaro, A., Zeyer, J., Kretzschmar, R., 2011. Influence of arsenate adsorption to ferrihydrite, goethite, and boehmite on the kinetics of arsenate reduction by Shewanella putrefaciens strain CN-32. Environ. Sci. Technol. 45, 7701–7709.
Jambor, J.L., Dutrizac, J.E., 1998. Occurrence and constitution of natural and synthetic ferrihydrite, a widespread iron oxyhydroxide. Chem. Rev. 98, 2549–2585.
Janney, D.E., Cowley, J.M., Buseck, P.R., 2000. Transmission electron microscopy of synthetic 2- and 6-line ferrihydrite. Clays Clay Miner. 48, 111–119.
Jia, Y., Xu, L., Fang, Z., Demopoulos, G., 2006. Observation of surface precipitation of arsenate on ferrihydrite. Environ. Sci. Technol. 40, 3248–3253.
Jia, Y., Xu, L., Wang, X., Demopoulos, G.P., 2007. Infrared spectroscopic and X-ray diffraction characterization of the nature of adsorbed arsenate on ferrihydrite. Geochim. Cosmochim. Acta 71, 1643–1654.
Jiang, X., Peng, C., Fu, D., Chen, Z., Shen, L., Li, Q., Ouyang, T., Wang, Y., 2015. Removal of arsenate by ferrihydrite via surface complexation and surface precipitation. Appl. Surf. Sci. 353, 1087–1094.
Kong, M., Li, Y., Chen, X., Tian, T., Fang, P., Zheng, F., Zhao, X., 2011. Tuning the relative concentration ratio of bulk defects to surface defects in TiO_2 nanocrystals leads to high photocatalytic efficiency. J. Am. Chem. Soc. 133, 16414–16417.
Kresse, G., Joubert, D., 1999. From ultrasoft pseudopotentials to the projector augmented-wave method. Phys. Rev. B 59, 1758.
Lan, S., Ying, H., Wang, X., Liu, F., Tan, W., Huang, Q., Zhang, J., Feng, X., 2018. Efficient catalytic As(III) oxidation on the surface of ferrihydrite in the presence of aqueous Mn(II). Wat. Res. 128, 92–101.
Leaist, D., 2007. Mutual diffusion coefficients for binary aqueous solutions of arsenous, arsenic, and malonic acids. J. Chem. Eng. Data 52, 1319–1325.
Li, Y., Chan, T., Jing, C., 2020. Arsenic adsorption on hematite facets: spectroscopy and DFT study. Environ. Sci. Nano 7, 3927–3939.
Li, X., He, K., Pan, B., Zhang, S., Lu, L., Zhang, W., 2012. Efficient As(III) removal by macroporous anion exchanger-supported Fe-Mn binary oxide: Behavior and mechanism. Chem. Eng. J. 193–194, 131–138.
Liu, L., Tan, W., Suib, S.L., Qiu, G., Zheng, L., Su, S., 2019. Enhanced adsorption removal of arsenic from mining wastewater using birnessite under electrochemical redox reactions. Chem. Eng. J. 375, 122051.
Liu, C., Yu, H., Liu, C., Li, F., Xu, X., Wang, Q., 2015. Arsenic availability in rice from a mining area: Is amorphous iron oxide-bound arsenic a source or sink? Environ. Pollut. 199, 95–101.
Liu, X., Zhou, K., Wang, L., Wang, B., Li, Y., 2009. Oxygen vacancy clusters promoting reducibility and activity of ceria nanorods. J. Am. Chem. Soc. 131, 3140–3141.
Maillot, F., Morin, G., Wang, Y., Bonnin, D., Ildefonse, P., Chaneac, C., Calas, G., 2011. New insight into the structure of nanocrystalline ferrihydrite: EXAFS evidence for tetrahedrally coordinated iron(III). Geochim. Cosmochim. Acta 75, 2708–2720.
Majzlan, J., Plášil, J., Škoda, R., Gescher, J., Kögler, F., Rusznyak, A., Küsel, K., Neu, T.R., Mangold, S., Rothe, J., 2014. Arsenic-rich acid mine water with extreme arsenic concentration: Mineralogy, geochemistry, microbiology, and environmental implications. Environ. Sci. Technol. 48, 13685–13693.
Maliyekkal, S.M., Philip, L., Pradeep, T., 2009. As(III) removal from drinking water using manganese oxide-coated-alumina: Performance evaluation and mechanistic details of surface binding. Chem. Eng. J. 153, 101–107.
Manning, B., Fendorf, S., Goldberg, S., 1998. Surface structures and stability of arsenic(III) on goethite: Spectroscopic evidence for inner-sphere complexes. Environ. Sci. Technol. 32, 2383–2388.
Manning, B.A., Fendorf, S.E., Bostick, B., Suarez, D.L., 2002. Arsenic(III) oxidation and arsenic(V) adsorption reactions on synthetic birnessite. Environ. Sci. Technol. 36, 976–981.
Meng, X., Korfiatis, G.P., Bang, S., Bang, K.W., 2002. Combined effects of anions on arsenic removal by iron hydroxides. Toxicol. Lett. 133, 103–111.
Michel, M., Ehm, L., Antao, S., Lee, P., Chupas, P., Liu, G., Strongin, D., Schoonen, M., Phillips, B., Parise, J., 2007. The structure of ferrihydrite, a nanocrystalline material. Science 316, 1726–1729.
Muller, K., Ciminelli, V., Dantas, M., Willscher, S., 2010. A comparative study of As (III) and As(V) in aqueous solutions and adsorbed on iron oxy-hydroxides by Raman spectroscopy. Wat. Res. 44, 5660–5672.
Nagai, Y., Takadate, K., Tang, Z., Ohkubo, H., Sunaga, H., Takizawa, H., Hasegawa, M., 2003. Positron annihilation study of vacancy-solute complex evolution in Fe-based alloys. Phys. Rev. B 67, 224202.
Neumann, A., Kaegi, R., Voegelin, A., Hussam, A., Munir, A.K.M., Hug, S.J., 2013. Arsenic removal with composite iron matrix filters in Bangladesh: A field and laboratory study. Environ. Sci. Technol. 47, 4544–4554.
Ona-nguema, G., Morin, G., Juillot, F., Calas, G., Brown, G., 2005. EXAFS analysis of arsenite adsorption onto two-line ferrihydrite, hematite, goethite, and lepidocrocite. Environ. Sci. Technol. 39, 9147–9155.
Parkinson, G.S., 2016. Iron oxide surfaces. Surf. Sci. Rep. 71, 272–365.
Perdew, J.P., Burke, K., Ernzerhof, M., 1996. Generalized gradient approximation made simple. Phys. Rev. Lett. 77, 3865.
Qi, P., Pichler, T., 2014. Closer look at As(III) and As(V) adsorption onto ferrihydrite under competitive conditions. Langmuir, 11110–11116.
Qi, P., Pichler, T., 2016. Competitive adsorption of As(III) and As(V) by ferrihydrite: equilibrium, kinetics, and surface complexation. Water, Air, Soil Pollut. 227, 1–9.
Qiu, H., Lv, L., Pan, B.C., Zhang, Q.J., Zhang, W.M., Zhang, Q.X., 2009. Critical review in adsorption kinetic models. J. Zhejiang Univ. Sci. A 10, 716–724.
Raven, K.P., Jain, A., Loeppert, R.H., 1998. Arsenite and arsenate adsorption on ferrihydrite: kinetics, equilibrium, and adsorption envelopes. Environ. Sci. Technol. 32, 344–349.
Revellame, E.D., Fortela, D.L., Sharp, W., Hernandez, R., Zappi, M.E., 2020. Adsorption kinetic modeling using pseudo-first order and pseudo-second order rate laws: A review. Clean. Eng. Technol. 1, 100032.
Schindler, M., Schreckenbach, M., Akbari Alavijeh, M., Wirth, M.G., Qafoku, O., Kovarik, L., Perea, D.E., 2022. Deciphering the distribution and crystal-chemical environment of arsenic, lead, silica, phosphorus, tin, and zinc in a porous ferrihydrite grain using transmission electron microscopy and atom probe tomography. ACS Earth Space Chem. 6, 558–570.
Schwertmann, U., Cornell, R.M., 2000. Iron Oxides in the Laboratory: Preparation and Characterization. WILEY-VCH Verlag GmbH & Co. KGaA, Weinheim, pp. 104–105.
Shannon, R.D., Prewitt, C.T., 1969. Effective ionic radii in oxides and fluorides. Acta Crystallogr. B 25, 925–946.
Simonin, J.P., 2016. On the comparison of pseudo-first order and pseudo-second order rate laws in the modeling of adsorption kinetics. Chem. Eng. J. 300, 254–263.
Sudhakar, C., Kumar, A.A., Bhuin, R.G., Gupta, S.S., Natarajan, G., Pradeep, T., 2018. Species-specific uptake of arsenic on confined metastable 2–Line-ferrihydrite: A combined Raman-X-ray photoelectron spectroscopy investigation of the adsorption mechanism. ACS Sustainable Chem. Eng. 6, 9990–10000.
Suresh, P., Korving, L., Keesman, K.J., Loosdrecht, M.C.M.V., Witkamp, G., 2019. Effect of pore size distribution and particle size of porous metal oxides on phosphate adsorption capacity and kinetics. Chem. Eng. J. 358, 160–169.
Takahashi, Y., Sakamitsu, M., Masato, T., 2011. Diffusion coefficients of arsenate and arsenite in water at various pH. Chem. Lett. 40, 1187–1188.
Tan, K.L., Hameed, B.H., 2017. Insight into the adsorption kinetics models for the removal of contaminants from aqueous solutions. J. Taiwan Inst. Chem. Eng. 74, 25–48.
Tan, W., Liang, Y., Xu, Y., Wang, M., 2022. Structural-controlled formation of nano-particle hematite and their removal performance for heavy metal ions: A review. Chemosphere 306, 135540.
Tang, W., Li, Q., Gao, S., Ku, J., 2011. Arsenic(III, V) removal from aqueous solution by ultrafine α-Fe_2O_3 nanoparticles synthesized from solvent thermal method. J. Hazard. Mater. 192, 131–138.
Tobler, D.J., Thomas, A.N., Freeman, H.M., Dideriksen, K., Radnik, J., Benning, L.G., 2019. Adsorption and reduction of arsenate during the Fe^{2+}-induced transformation of ferrihydrite. ACS Earth Space Chem. 3, 884–894.
Valderrama, C., Gamisans, X., de las Heras, X., Farrán, A., Cortina, J.L., 2008. Sorption kinetics of polycyclic aromatic hydrocarbons removal using granular activated carbon: Intraparticle diffusion coefficients. J. Hazard. Mater. 157, 386–396.
Villacís-garcía, M., Ugalde-arzate, M., Vaca-escobar, K., Villalobos, M., Zanella, R., Martínez-villegas, N., 2015. Laboratory synthesis of goethite and ferrihydrite of controlled particle sizes. B. Soc. Geol Mex. 67, 433–446.
Villalobos, M., Escobar-Quiroz, I.N., Salazar-Camacho, C., 2014. The influence of particle size and structure on the sorption and oxidation behavior of birnessite: I. Adsorption of As(V) and oxidation of As(III). Geochim. Cosmochim. Acta 125, 564–581.
Wang, X., Liu, F., Tan, W., Li, W., Feng, X., Sparks, D.L., 2013. Characteristics of phosphate adsorption-desorption onto ferrihydrite: comparison with well-crystalline Fe (hydr)oxides. Soil Sci. 178, 1–11.
Wang, X., Zhu, M., Koopal, L.K., Li, W., Xu, W., Liu, F., Zhang, J., Liu, Q., Feng, X., Sparks, D.L., 2016. Effects of crystallite size on the structure and magnetism of ferrihydrite. Environ. Sci. Nano 3, 190–202.
Waychunas, G.A., Rea, B.A., Fuller, C.C., Davis, J.A., 1993. Surface chemistry of ferrihydrite: Part 1. EXAFS studies of the geometry of coprecipitated and adsorbed arsenate. Geochim. Cosmochim. Acta 57, 2251–2269.
Waychunas, G.A., Fuller, C.C., Davis, J.A., 1996. Wide angle X-ray scattering (WAXS) of arsenate sorption and counterion study of "two-line" ferrihydrite structure: Effect variation and comparison with EXAFS results. Geochim. Cosmochim. Acta 60, 1765–1781.
Weatherill, J.S., Morris, K., Bots, P., Stawski, T.M., Janssen, A., Abrahamsen, L., Blackham, R., Shaw, S., 2016. Ferrihydrite formation: The Role of Fe13 Keggin clusters. Environ. Sci. Technol. 50, 9333–9342.
Weber, K.A., Achenbach, L.A., Coates, J.D., 2006. Microorganisms pumping iron: Anaerobic microbial iron oxidation and reduction. Nat. Rev. Microbiol. 4, 752–764.
Yang, X., Xia, L., Li, J., Dai, M., Yang, G., Song, S., 2017. Adsorption of As(III) on porous hematite synthesized from goethite concentrate. Chemosphere 169, 188–193.

Zhang, H.J., Chen, Z.Q., Wang, S.J., 2010. Spin conversion of positronium in NiO/Al_2O_3 catalysts observed by coincidence Doppler broadening technique. Phys. Rev. B 82, 035439.
Zhang, G., Qu, J., Liu, H., Liu, R., Guoping, L., 2007a. Removal mechanism of As(III) by a novel Fe−Mn binary oxide adsorbent oxidation and sorption. Environ. Sci. Technol. 41, 4613–4619.
Zhang, G., Qu, J., Liu, H., Liu, R., Wu, R., 2007b. Preparation and evaluation of a novel Fe-Mn binary oxide adsorbent for effective arsenite removal. Wat. Res. 41, 1921–1928.
Zhang, G., Liu, H., Qu, J., Jefferson, W., 2012. Arsenate uptake and arsenite simultaneous sorption and oxidation by Fe-Mn binary oxides: Influence of Mn/Fe ratio, pH, Ca^{2+}, and humic acid. J. Colloid Interface Sci. 366, 141–146.
Zhang, G., Liu, F., Liu, H., Qu, J., Liu, R., 2014. Respective role of Fe and Mn oxide contents for arsenic sorption in iron and manganese binary oxide: An X-ray absorption spectroscopy investigation. Environ. Sci. Technol. 48, 10316–10322.
Zhao, Z., Jia, Y., Xu, L., Zhao, S., 2011. Adsorption and heterogeneous oxidation of As (III) on ferrihydrite. Wat. Res. 45, 6496–6504.
Zheng, Q., Hou, J., Hartley, W., Ren, L., Wang, M., Tu, S., Tan, W., 2020. As(III) adsorption on Fe-Mn binary oxides: Are Fe and Mn oxides synergistic or antagonistic for arsenic removal? Chem. Eng. J. 389, 124470.
Zheng, Q., Tu, S., Hou, J., Ni, C., Wang, M., Ren, L., Wang, M., Cao, M., Xiong, S., Tan, W., 2021. Insights into the underlying mechanisms of stability working for As (III) removal by Fe-Mn binary oxide as a highly efficient adsorbent. Wat. Res. 203, 117558.
Zhu, J., Pigna, M., Cozzolino, V., Caporale, A.G., Violante, A., 2011. Sorption of arsenite and arsenate on ferrihydrite: Effect of organic and inorganic ligands. J. Hazard. Mater. 189, 564–571.
Zhu, Y., Xue, X., Kappler, A., Rosen, B.P., Meharg, A.A., 2017. Linking genes to microbial biogeochemical cycling : Lessons from arsenic. Environ. Sci. Technol. 51, 7326–7339.